Disaggregated anisotropy of the upper and lower crust and deformation style in the southeast margin of Tibet

Haiyan Yang[1], José Badal[2], Jiafu Hu[1]*, Hengchu Peng[1]

[1]Department of Geophysics, Yunnan University, 2 North Green Lake Rd., Kunming, Yunnan, 650091 P.R. China, jfhu@ynu.edu.cn

[2]Physics of the Earth, Sciences B, University of Zaragoza, Pedro Cerbuna 12, 50009 Zaragoza, Spain, badal@unizar.es

*Corresponding author: Jiafu Hu, email: jfhu@ynu.edu.cn

Abstract

The arrival times of the converted P-to-S phase at an intracrustal discontinuity (Pis) or at the Moho (Pms) provide a powerful diagnostic tool for detecting anisotropy with horizontal symmetry axis. In this study, we use Pis and Pms arrival times extracted from P receiver functions to determine by shear wave splitting the anisotropy of the upper and lower crust separately in the southeast margin of Tibet. As far as our knowledge is concerned, it is the first time that such a study deals with disaggregating the anisotropy of the upper crust from the lower one in the SE of Tibet. The instrument network consisted of 285 temporary broadband stations plus 3 permanent stations deployed in Yunnan and adjacent areas, which recorded 278 teleseismic events with Ms ≥ 5.8. Once the receiver functions were calculated, we follow a two-stage work scheme: first we measure the splitting parameters of the upper crust by fitting the Pis-phase arrival time, and then, after correcting for the effect of the anisotropic upper crust on the Pms arrival, we adjust the

Pms-phase arrival to obtain the splitting parameters of the lower crust. In this way, we achieved 75 double-layer splitting measurements. In the upper crust, the delay times vary between 0.05 s and 1.34 s with an average of 0.53 s ± 0.29 s, while they range from 0.06 s to 1.42 s with an average of 0.62 s ± 0.33 s in the lower crust. In addition to the existence of a wide intracrustal low-velocity zone, the results confirm that the upper crust and the lower crust are decoupled anisotropic structures in the SE margin of Tibet. In the upper crust, the fast wave polarization directions show a clockwise rotation around the Eastern Himalayan Syntax, suggesting that the extensional fluid-saturated microcracks induced by rigid extrusion from central Tibet are mostly responsible for the observed anisotropy. In contrast, the lattice preferred orientation of anisotropic minerals induced by a channel flow seems to be the main cause of the detected anisotropy in the lower crust.

Keywords: Ps-wave splitting; double-layer crustal anisotropy; layer-stripping technique; crustal deformation mechanism; southeast Tibet.

1. Introduction

The India-Eurasia continental collision occurred ~70Ma ago is the most spectacular example of mountain building and plateau development, which has caused at least a shortening of the crust of about 1400 km (Yin & Harrison, 2000). The southeast margin of Tibet is particularly important for understanding the expansion of the Tibetan Plateau. The area is located at the transition zone between the heartland of the plateau (average elevation of 4500 m) and the South China block (Fig. 1a). The crustal thickness varies dramatically from ~60 km in the Songpan-Ganzi fold system and the northern part of the Sichuan-Yunnan diamond-shaped block (SYDSB), near the Eastern Himalayan Syntax

(EHS), to ~33 km in southern Yunnan (Hu et al., 2018). This feature reveals that the crust in the southeast margin of Tibet has undergone a strong tectonic deformation during the Indo-Asian collision (Molnar & Tapponnier, 1975; England & Molnar, 1997; England & Houseman, 1988; Yin, 2000). This process of continental deformation seems to accommodate by a lateral rigid extrusion along great strike-slip faults, such as the Xianshuihe-Xiaojiang fault, Jinshajiang-Red River fault and Sagaing fault (Molnar & Tapponnier, 1975; Tapponnier et al., 1982, 1990, 2001; Yin & Harrison, 2000). These faults divide the study region into the Tengchong-Baoshan Block (TBB), the Central Yunnan Block (CYB), the Eastern Yunnan Block (EYB) and the Lanping-Simao Block (LSB) (Wang et al., 1998, 2014) (Fig. 1b).

GPS observations have confirmed that crustal materials are moving southeastward and undergoing a clockwise rotation around the Eastern Himalayan Syntax (Zhang et al., 2004; Gan et al., 2007). Undoubtedly, the surface geological features and the GPS data provide direct constraints on the surface deformation, even on the shallow crust, but not for the whole crust, in particular for the middle-to-lower crust. Two end-member models including lateral extrusion of rigid blocks and lower crust flow have been proposed to explain the mechanism responsible for the expansion and uplift in the southeast margin of Tibet (Molnar & Tapponnier, 1975; Tapponnier et al., 1982; Royden et al., 1997; Clark & Royden, 2000). The lower crustal flow model is a popular model because it offers a reasonable interpretation of the surface deformation and mountain building in eastern Tibet (Royden et al., 1997; Clark & Royden, 2000). The hypothesis is that lower crustal flow inflated the crust by injecting mechanically weak lithospheric material coming from central Tibet, so that there are no major crustal thrust faults in the SE margin of Tibet (Klemperer, 2006; Royden et al., 2008). However, this still raises some controversy and is the subject of lively debate due to the lack of definitive evidence. For instance, the lateral extrusion model of rigid blocks proposed that deformation occurred primarily along strike-slip faults that bound the blocks (Molnar & Tapponnier, 1975; Tapponnier et al., 1982); but it cannot give a reasonable interpretation to the earthquakes occurred inside of blocks. The lower crustal flow model assumed that there exists a mechanically weak layer extended widely within the middle-to-lower crust (Royden et al., 1997; Clark & Royden, 2000); however, later studies (Bai et al, 2010; Bao et al., 2015) argued that the lower crustal flow runs along two arc-shaped channels along the Xianshuihe-Xiaojiang fault and Jiali-Nujiang fault (Fig. 1a). On the other hand, some researchers disagree that the lower crustal flow has penetrated through the Jinshajiang-Red River fault and has extended to the Indochina block (Zheng et al., 2017; Hu et al., 2018).

In this study, we address the problem from the point of view of the anisotropy structure. Since the pervasive deformation of the rocks can produce anisotropy at the seismic wavelength scale (Mainprice & Nicolas, 1989), the seismic anisotropy can in turn provide important constraints on the geodynamic models for the lifting and lateral expansion of the Tibetan Plateau. Many studies based on SKS/SKKS splitting have focused on the anisotropy and deformation of the crust and mantle in eastern Tibet (Flesch et al., 2005; Lev et al., 2006; Sol et al., 2007; Levin et al., 2008; Wang et al., 2008; Chang et al., 2015). Nevertheless, shear wave splitting (hereafter SWS) offers excellent lateral resolution but poor vertical resolution (Savage, 1999). Unlike the converted phase at the core-mantle boundary, the Moho converted Pms phase is strictly confined in the crust and therefore can provide valuable knowledge about the deformation of the crust (Chen et al., 2013). In the SE margin of Tibet, Pms splitting parameters obtained from receiver functions recorded by sparse seismic networks have provided valuable information on the structure and deformation of the crust (Sun et al., 2012, 2015; Chen et al., 2013; Yang et al. 2015; Cai et al., 2016; Kong et al., 2016). However, there are considerable discrepancies in both the fast wave polarization direction and the delay time. In addition to these discrepancies, another issue arises in relation to the source of anisotropy, since there are results that speculate that the source causing Pms splitting in the SE margin of Tibet should be attributed mainly to the middle and lower crust flow, in any case below 15 km depth (Cai et al., 2016; Sun et al., 2012, 2015).

We are interested in investigating the anisotropy of the upper crust separately from that of the lower crust; but the reality is that Pms-wave splitting is due to the anisotropy of the upper crust or the lower crust, or of these two layers together. Pms splitting provides only one pair of splitting parameters (fast wave polarization direction and delay time) concerning the entire crust, which must be considered as apparent values to the extent that they are the result of the superposition of the effects of the individual layers rather than a simple sum of splitting parameters (Rümpker et al., 2014). In order to investigate the deformation mechanism of the crust in the southeast margin of Tibet, we use the layer-stripping technique (Rümpker et al., 2014) to obtain the anisotropic parameters corresponding to the upper and lower crust from P receiver functions (PRFs) recorded at the same array stations used by Cai et al (2016) and in three permanent stations more.

2. Data and method

2.1. Data acquisition and routine operations

We use seismic data recorded by 285 seismographs deployed in Yunnan and adjacent areas in the framework of the ChinArray program and 3 other permanent stations (Fig. 1b). These stations were equipped with seismometers CMG-40T or CMG-3ESPC and installed with an average spacing between stations of ~35 km by the China Earthquake Administration and the Nanjing University. They were in operation from June 2011 to November 2013 and are the same stations used by Cai et al. (2016) to obtain Pms wave splitting measurements. We collected 278 teleseismic events with Ms ≥ 5.8 and epicentral distances between 30º and 95º (Fig. 1c) for further computation of PRFs.

In practice, the ZNE displacement components are rotated to the LQT ray-coordinate system, so that the longitudinal Pp wave is polarized on the L component while the transversal Ps wave is polarized on the Q component. Theoretically, the effects due to the seismic source and seismic path traveled by the waves can be removed from the seismograms by deconvolution (Vinnik, 1977; Langston, 1977, 1979). We use a controlled-bandwidth Gaussian filter to low-pass filter the signal components through the parameter that controls the bandwidth of the filter that we set to be 2.0. (Ammon, 1991). Next, we isolate the converted Ps phase from PRFs by iterative time-domain deconvolution of the L component from the Q component (Ligorria & Ammon, 1999; Peng et al., 2019). To ensure receiver functions with high signal-to-noise ratio (SNR), we discard the waveforms with SNR<5. Finally, we gathered 43060 PRFs.

For a given discontinuity, the arrival time of the converted Ps wave is a function of the incidence angle controlled by the slowness. In order to eliminate the dependence of the arrival time on the epicentral distance and the slowness, all individual PRFs were moveout corrected to a reference epicentral distance of 67º (Dueker et al., 1997, 1998) using the IASP91 model (Kennett & Engdahl, 1991) and then stacked in a single trace to obtain the Ps arrival time.

2.2. Two-layer anisotropy versus single-layer anisotropy

Let´s reproduce the theory briefly. Assuming a single anisotropic layer with horizontal symmetry axis, the converted Ps-phase arrival time varies systematically with the back-azimuth of the seismic source and can be expressed as follow (Rümpker et al., 2014):

$$t_{Ps} = t_0 + \Delta t = t_0 - \frac{\delta t}{2}\cos[2(\theta - \varphi)] \tag{1}$$

where t_0 is the Ps arrival time in the isotropic case and Δt is the offset caused by crustal anisotropy along the raypath; δt and φ are the splitting parameters, i.e. the delay time between the fast and slow waves and the fast-wave polarization direction (hereafter abbreviated by FPD), respectively; θ is the back-azimuth of the incident ray measured clockwise from the north. This equation indicates that the anisotropy obeys to a characteristic degree-2 (180º-periodic) back-azimuth pattern in travel times (Vera & Mahan, 2014). The classical splitting parameters can be obtained by fitting the Ps arrival time using the grid-search scheme, which consists of finding the optimal combination of t_0, δt and φ that gives the minimum difference between the observed and predicted arrival times:

$$S(\delta t, \varphi) = \sum_{i=1}^{N} \left(t_{Ps}^{(i)}(\delta t, \varphi) - t_{Obs}^{(i)}\right)^2 \tag{2}$$

where N is the total number of PRFs, and $t_{\mathrm{Obs}}^{(i)}$ and $t_{Ps}^{(i)}$ denote respectively the observed and predicted Ps arrival times in the i-*th* waveform. When $S(\delta t, \varphi)$ reaches the minimum value on the solution surface, the values of δt and φ become the optimal splitting parameters. Uncertainties affecting the splitting parameters can be estimated from the flatness of $S(\delta t, \varphi)$ around the minimum, as described by Zhu & Kanamori (2000).

In the case of two anisotropic layers with different splitting parameters, we assume that the Ps_1 phase is generated at the base of the upper layer, while the Ps_2 phase is generated at the base of the lower layer. For a weakly anisotropic medium, the combined effect of the two layers can be approximated by the summation of moveouts in both layers (Rümpker et al., 2014):

$$\Delta t_{1,2} = \Delta t_1 + \Delta t_2 \tag{3}$$

where the subscripts of 1 and 2 denote upper layer and lower layer, respectively. The total moveout for the Ps_2 phase can be expressed by:

$$\Delta t_{1,2} = -\frac{\delta t_{1,2}}{2}\cos[2(\theta - \varphi_{1,2})] \tag{4}$$

where $\delta t_{1,2}$ and $\varphi_{1,2}$ denote the apparent splitting parameters of the two anisotropic layers, whose respective expressions are:

$$\delta t_{1,2} = \sqrt{\delta t_1{}^2 + \delta t_2{}^2 + 2\delta t_1 \delta t_2 \cos[2(\varphi_1 - \varphi_2)]} \tag{5}$$

$$\tan(\phi_{1,2}) = \frac{\delta t_1 \sin(2\varphi_1) + \delta t_2 \sin(2\varphi_2)}{\delta t_1 \cos(2\varphi_1) + \delta t_2 \cos(2\varphi_2)} \tag{6}$$

These equations indicate that the total effect of the two anisotropic layers is given by the effects of the individual layers, instead of a simple summation of splitting parameters. We obtain the splitting parameters of the upper layer by fitting the Ps_1 phase arrival time (as in the single-layer case described above); then we remove the effect of the upper layer on the Ps_2 phase arrival time by subtracting Δt_1 in equation (3). After correcting for the anisotropy of the upper layer, the anisotropic parameters of lower layer are obtained by fitting the Ps_2 phase arrival time. This procedure is called layer-stripping technique.

3. Results

3.1. Double-layer crustal anisotropy

In Fig. 2 we show the receiver functions obtained at station 53133 (Fig. 2a) together with an enlarged view of the arrival times of the Pms peaks (Fig. 2b). Based on previous knowledge of the crustal thickness (Bao et al., 2015; Hu et al., 2018), the Pms phase should occur at ~5 s in southern Yunnan. To obtain the anisotropic parameters of the crust, the arrival time t_0 was set to 4.8 s in equation (1) to then allow a sweeping within the interval from t_0–0.5 s to t_0+0.5 s with step of 0.1 s. So, for a given value of t_0, a candidate solution can be obtained by following the aforementioned grid-search scheme. After repeating this procedure, the optimal solution given by the smallest squared difference (2) is selected from the series of candidate solutions. Thus we obtained the pair of splitting parameters 0.66±0.08 s and –66±4° (Fig. 2c). The theoretical arrival times computed from the splitting parameters fit well the observed arrival times of the Pms phase (Fig. 2b). Unfortunately, although there is a converted P-to-S phase at an intracrustal interface in the azimuthal gather of receiver functions (Fig. 2a), it cannot be used to estimate the anisotropy of the upper crust due to the poor coherence in polarity.

To obtain robust two-layer crustal anisotropy measurements, the following preconditions must be met: (1) existence of an intracrustal discontinuity with a marked contrast of seismic velocity; (2) clear and azimuthally varying Pis arrival times; (3) high-quality receiver functions with good azimuthal coverage. Now we present the results obtained at station 53216 installed near to the Xianshuihe-Xiaojiang fault, where a big Ms=8 magnitude earthquake occurred in 1833, suggesting a strong deformation of the crust. We can see two converted phases with distinct polarity (Fig. 3a): one negative (the Pis phase) at ~2.1 s and another positive (the Pms phase) at ~5.0 s that does not exhibit azimuthal dependence. The average arrival time t_0 was set to 5.1 s, and we obtained the pair of Pms splitting parameters 0.25±0.06 s and 57±6º (Fig. 3b). In principle, this result reveals a weak anisotropic crust. However, the intracrustal phase after the direct P-wave (at ~2.1 s) exhibits a significant azimuthal dependence (Fig. 3a), so that we fitted the arrival time for obtaining the anisotropy in the upper crust and obtained the splitting parameters 0.97±0.09 s and –34±2º (Fig. 3c). As can be seen, the theoretical Pis-phase arrival time computed from the previous anisotropic parameters fits well the observed arrival time (Fig. 3c). In this case we can remove the effect of the anisotropic upper crust on the Moho converted Pms phase by subtracting the time Δt_1 from the observed total moveout $\Delta t_{1,2}$ of the Pms phase. After correcting for upper crust anisotropy by layer stripping, the Pms arrival time exhibits a characteristic degree-2 back-azimuth pattern (Fig. 3d). Then we fitted again the Pms arrival time and we finally obtained the splitting parameters 1.27±0.10 s and 55±2º (Fig. 3d), implying that the lower crust is highly anisotropic. This example demonstrates that the apparent splitting parameters do not reflect the crustal anisotropy correctly when FPD (55º) in the lower crust is almost perpendicular to FPD (–34º) in the upper crust.

As another example of two-layer crustal anisotropy measurement, we present the results at station 51010. In contrast with station 53216, the Pis phase shows a positive polarity and exhibits a very weak azimuthal dependence, while the Pms phase exhibits an obvious azimuthal dependence (Fig. 3e). The splitting parameters 0.76±0.09 s and 48±3º obtained by fitting the original Pms-phase arrivals (Fig. 3f), suggest that the crust is apparently highly anisotropic. Adjusting the Pis-phase arrival time, the splitting parameters of the upper crust are 0.47±0.07 s and 48±4º (Fig. 3g); then, after removing the anisotropy of the upper crust, we finally obtained the splitting parameters of the lower crust 0.21±0.06 s and 44±7º (Fig. 3h). This result makes clear that the upper crust is comparatively more anisotropic than the lower crust, so we should not simply attribute the anisotropy source causing the Pms phase splitting to the lower crust as in previous studies (Sun et al., 2012, 2015; Cai et al., 2016).

Lastly, we obtained 275 pairs of Pms-splitting-values for crustal anisotropy (Fig. S1). The delay times vary between 0.08 s and 1.44 s, with an average of 0.50±0.27 s. For the set of stations that met the established preconditions, we applied the disaggregation method described above and obtained a total of 75 disaggregated anisotropy parameters estimated by Pis and Pms splitting for the upper and lower crust (Table 1). In the upper crust, the delay time ranges from 0.05 s to 1.34 s, with an average of 0.53±0.29 s, while in the lower crust the splitting time varies from 0.06 s to 1.42 s, with an average of 0.62±0.33 s. This suggests the existence of a relevant shear zone in the lower crust. The averaged SWS parameters that characterize the disaggregated anisotropy of the upper and lower crust in different tectonic units are listed in Table 2.

3.2. Upper crust thickness

The Pis-phase splitting delay time in relation to the direct P-wave provides essential information to tightly constraint the depth of the intracrustal discontinuity where the phase originates. For a given discontinuity at a depth *d*, the arrival time of the converted Ps-phase is given by (Dueker et al., 1997, 1998):

$$T_{Pds} = \int_{-d}^{0} \left(\sqrt{V_s^{-2} - p^2} - \sqrt{V_p^{-2} - p^2}\right) dz \qquad (7)$$

where Vp and Vs denote the velocities of the P and S waves, respectively, z is depth, and p is the ray parameter. In this equation, the arrival time obviously depends on the slowness (or epicentral distance). Based on the IASP91 model (Kennett & Engdahl, 1991), we can calculate the curve that defines the relationship between the conversion depth and the arrival time of the converted P-to-S wave for given a ray parameter, so that the depth of the upper crust can be obtained from this curve once the Pis-phase arrival time is given.

We must emphasize that our interest is focused on the first converted phase behind the direct P-wave; and the reason is that the reverberations at the intracrustal interface can mask other converted phases and hinder its identification. The recognition or not of the Pis-phase depends on the following criteria: (1) the coherence of the first converted phase arriving behind the direct P-wave in the individual receiver functions and in the stacked trace; (2) the amplitude of the converted phase in the stacked trace that must be above the 95% confidence limit, i.e. must exceed the $\pm 2\sigma$ error limit (see online supplementary material and Fig. S2). We obtained 153 Pis-phase delay time measurements in the range of 1.66-3.08 s with an average value of 2.42 s. Based on the IASP91 model (Kennett & Engdahl, 1991), we converted the time data into depth data (Dueker et al., 1997, 1998) to obtain the upper crust thickness in the study area. Fig. 4 shows the results mapped by isolines drawn at 3 km intervals. The upper crust thickness varies from ~15 km in TBB and LSB to ~21 km in CYB, and decreases rapidly eastward up to 15-18 km in EYB across the Xiaojiang fault.

The Pis-phase polarity (which in Fig. 4 can be distinguished by the color of the triangles that indicate the locations of the array stations) also provides an important constraint on the seismic impedance below the intracrustal discontinuity. Thus, the observed negative polarity indicates that a wide low-velocity zone seems to spread from CYB to EYB across the Xiaojiang fault, and toward LSB and TBB across the Jinshajiang-Red River fault.

3.3. Pis and Pms splitting vectors and stress field

In Fig. 5a, we present the focal mechanism solutions calculated for earthquakes with Ms ≥ 4.0 that have occurred in the southeast of Tibet since 1965 AD to 2017. This allows us to determine the maximum horizontal compression stress by stress-field inversion for different tectonic blocks and compare with the FPDs given by splitting analysis. Fig. 5b shows the maximum compression stress for different tectonic blocks (black rose diagrams) together with the Pis and Pms splitting vectors and the respective rose diagrams. What first draws attention is that the SWS directions in the upper crust estimated by Pis splitting (red bars) clearly differ from those of the disaggregated anisotropy in the lower crust measured by Pms splitting (blue bars), which means two layers with a differentiated anisotropy regime.

4. Discussion

4.1. About the splitting measurements

Four wide-angle seismic profiles reveal that the crust in the Yunnan region can be roughly divided into upper, middle and lower crust (Zhang and Wang, 2009), but this stratification is only observed in some stations (Fig. S2). For this reason and for the sake of simplicity we have considered a two-layer crustal model for our analysis. Nonetheless, the fact that only one robust Pis phase is observed in most stations suggests the existence of a fairly defined intracrustal interface in Yunnan.

On the other hand, it is true that there is an event gap in the azimuthal range 190º-260º (Fig. 1c), so this gap could yield uncertainty in the results. Even so, the azimuthal coverage of incident seismic rays does not involve any impediment to gather a sufficient number of clear intracrustal phases and reliable SWS parameters.

Unlike previous studies (Sun et al., 2012, 2015; Chen et al., 2013; Cai et al., 2016; Kong et al., 2016), this study is aimed to quantify the upper and lower crustal anisotropy separately under the assumption of a horizontal symmetry axis and a flat interface. The periodic variation of the Ps arrivals with the back-azimuth reveals as a useful diagnostic tool for azimuthal anisotropy (Vera & Mahan, 2014). The technique employed in this study assumes that an anisotropic structure with a horizontal axis of symmetry causes Ps-wave splitting. Synthetic results indicate that the tilted axis (30º) has a clear effect on the radial and transverse components of the Ps phase; however, its influence on the arrival time of the radial component is insignificant (Zheng et al., 2018). Furthermore, the Ps arrivals are easily picked up in the PRFs, so they can provide a robust method to adjust arrival times and obtain splitting parameters.

The FPDs deduced from the (non-disaggregated) Pms splitting parameters are quite similar to those obtained by Cai et al. (2016) using the same array (Fig. S1); but the average Pms splitting time of 0.28 s is smaller than ours. However, the average splitting time of ~0.50 s agrees with the delay time obtained at permanent stations (Sun et al., 2012, 2015; Yang et al., 2015; Wu et al., 2015; Wang et al., 2016; Zheng et al., 2018). The consistency of the crustal anisotropy estimations suggests that the assumption of horizontal axis is likely valid. The reason for the previous discrepancy in splitting time can simply be attributed to the method of analysis.

We assume that a single anisotropic layer with a horizontal axis of symmetry causes the converted P-to-S phase arrivals to show azimuthal variation as the cosine function. Theoretically, an azimuthal range of 180º can meet the adjustment conditions due to the presence of a degree-2 (180º-periodic) azimuthal variation in arrival times, even though the seismic events do not occur uniformly around the station. This does not avoid low SNR in the stacked trace along some particular azimuth. To obtain reliable division parameters, good azimuthal coverage of the incident rays is required. In addition, small-scale azimuthal variations in crustal velocity and a dipping Moho may affect the arrival times of the converted seismic phases. Therefore, it may be inappropriate to compare our results directly with those provided by previous studies, because there are many discrepancies in the data or stations.

Some previous studies used transverse receiver functions (Chen et al., 2013; Cai et al., 2016). The fact that the Pms arrivals on the transverse receiver functions have a much lower SNR than on the radial component, suggests that it is practically impossible to remove the anisotropy completely when the energy in the transverse component is corrected to its minimum value.

The splitting delay times in the lower crust vary from 0.06 s to 1.42 s with an average of 0.62 ±0.33 s. If we assume an average S-wave velocity of 3.6 km/s (Bao et al., 2015) and a ~20-km-thick layer, a supposed lower crust with 11% of azimuthal anisotropy could explain the splitting time of 0.62 s. Okaya et al. (1995) reported a high degree of anisotropy like this in lower crust schists. Mica and amphibole are also two candidate minerals to originate a strongly anisotropic crust; Tatham et al. (2008) found that amphibole can generate up to 13% of seismic anisotropy under strong shear conditions.

4.2. The Pis-phase and two-layer anisotropy

A strong contrast of seismic impedance, i.e. an abrupt jump in P- and S-wave velocity, as well as in density, is a clue of an intracrustal interface. A negative velocity gradient will generate a negative polarity phase at the top of the surface in the case of a near-vertically incident P wave, and vice versa. Similar to the results obtained from seismic soundings (Zhang and Wang, 2009), the observation of clear Pis arrivals in at least 153 stations suggests the existence of a generalized intracrustal interface, at least in Yunnan. In the other 125 stations, both positive and negative polarities at the same time window are observed along the azimuthal variation, so that the stacked amplitude of Pis is too weak to be distinguished (see Fig. 2S). GPS velocities (Zhang et al., 2004; Gan et al., 2007), strong shallow earthquakes caused by subsurface tectonic movements (Hu et al., 2018), shear wave splitting coming from local earthquakes confined in the depth range of 5-15 km (Shi et al., 2012), are features that suggest that the upper crust is remarkably anisotropic in the SE of Tibet. Although we achieved only 75 pairs of double-layer splitting measurements at 153 stations, the average splitting time of 0.53 s and 0.62 s in the upper and lower crust, respectively, demonstrates that both the upper and lower are highly anisotropic. Leaving aside the two-layer model, the fact is that the PRFs sample laterally a wide area, depending on the incident angle and azimuth of the ray. So a laterally heterogeneous structure would generate a converted phase, so that the Pis phase would have an inverse polarity when an incident P-wave coming from different azimuth arrives at the same station (Bao et al, 2015). In this case, we can use the Pis delay time relative to the direct P-wave to estimate the depth of the upper crust, but we cannot fit the arrival times to obtain the anisotropy parameters of the upper crust. Therefore, only with coherent and azimuthally varying Pis arrival times and a clear stacked trace, it is possible to apply the layer-stripping technique to obtain two-layer anisotropy. The existence of two-layer anisotropy is a questionable fact, as long as we do not have a method to isolate the anisotropy of both layers.

4.3. Upper crust anisotropy and compressional stress

A series of processes, such as fluid-filled fracture zones, vertical foliation planes containing anisotropic minerals, and mid/lower crustal flow that aligns anisotropic minerals, can result in crustal anisotropy. In general, it is believed that azimuthal anisotropy in the continental upper crust is mainly the result of the preferential orientation of fluid-saturated vertical cracks, and that the FPDs are sub-parallel to the direction of maximum horizontal compression (Crampin,1981). The strength of anisotropy depends on the tectonic setting and thickness of the anisotropic layer.

The upper crust in the SE margin of Tibet has undergone severe cracking due to the eastward extrusion of the Tibetan plateau (Tapponnier et al., 1982) and numerous active faults have developed (Allen et al., 1991; King et al., 1997). The upper crust is relatively hard and fragile, and most local earthquakes have occurred in the upper crust since 1965. Hence, the anisotropy of the upper crust can be the sum of comprehensive effects of major faults, crustal earthquakes and surface tectonic movements (Yang et al., 2015). For the upper layer of the crust, we have found delay times varying from 0.05 s to 1.34 s, with an average of 0.53±0.29 s, suggesting a remarkable anisotropy of the upper crust in the SE of Tibet. Previous studies suggest that the splitting time resulting from the preferred shape and orientation of fluid-saturated vertical cracks is normally less than 0.2 s (Crampin, 1994). Even for stations close to a fault zone, it is ~0.5 s (Savage et al., 1990), while the average splitting time for the upper crustal in the study area is 0.53 s, which seems to be too large. Shi et al. (2012) gave an average delay time of 1.8±1.2 ms/km from local SWS in the Yunnan area. Based on the fact that 93% of the earthquakes occurred in Yunnan are above a depth of 15 km, Cai et al. (2016) argued that the average cumulative splitting time within the top 15 km of the crust should be less than 0.045 s. Now, local SWS predominantly reflects the variation of the anisotropy along the ray path rather than the vertical variation. Zheng et al. (2018) performed 7 double layer anisotropy measurements and found a splitting time of 0.64 s for the upper crust in eastern Tibet, which is a value similar to ours. Unfortunately, there are few similar measurements to comparison with ours.

Mineral physics revealed that schists and gneisses, which are dominant in the exhumed middle continental crust, consist of flat, sheet-like minerals such as biotite, muscovite, chlorite, sericite, amphibole, talc and graphite; all of them have been considered as examples of typical mineral that cause anisotropy (Brocher and Christensen, 1990; Burlini and Fountain, 1993). In the SE margin of Tibet, schist, felsic gneiss and amphibolite are three major rocky constituents that occupy more than 95% of the metamorphic terranes of west Yunnan (Leloup et al., 1995; Tapponnier et al., 1982, 1990; Ji et al., 2000). A previous study (Ji et al., 2015) suggests that the crust, which contains 15-25 km thick schists, can contribute as much as 0.3-0.5 s to the observed delay times caused by shear wave splitting, which are comparable to the results obtained from Pms splitting.

The averaged FPDs in the upper crust vary from 103º in CYB to 98º in EYB (Table 2) indicating mainly direction E-W. A sharp contrast in FPDs arises in the Indochina block across the Jinshajiang-Red River fault, such that FPD goes from 103º in CYB to 77º in

TBB (Table 2), in line with the commonly accepted clockwise rotation around EHS (Fig. 5b). The regional compression stress field appears divided into two branches: one mainly oriented NW-SE east of the Jinshajiang-Red River fault and another that has rotated to N-S or NE-SW across the Jinshajiang-Red River fault in the Indochina block (Fig. 5b). This stress pattern is fully consistent with GPS vectors (Zhang et al., 2004; Gan et al., 2007). In the SE margin of Tibet, the FPDs in the upper crust are inconsistent with the strike of the active faults, but they are comparable to the maximum horizontal compression stress (Fig. 5b) and the GPS vectors. This last spatial consistency of the FPDs suggests that extensional fluid-saturated microcracks associated with the regional compression induced by the rigid extrusion of central Tibet, are primarily responsible for the observed anisotropy in the upper crust. In addition to the fluid-saturated microcracks, the contribution to anisotropy of the upper crust of mica- and amphibole-bearing rocks, such as schist, amphibolite, gneiss and mylonite, cannot be excluded.

SWS and the Pis-phase analysis can provide the anisotropy of the upper crust, but the origin of the anisotropy should be confined within the Fresnel zones along the geometric paths traveled by the analyzed shear waves. Thus, exactly, the fast polarization direction is the proxy of the anisotropy between source and the receiver, while that of the Pis-phase is between the conversion point that generated it and the receiver.

4.4. Evidence for lower crustal flow on the east side of the Jinshajiang-Red River fault

The high seismicity and thickening of the upper crust in CB (Fig. 4) indicate this area is very deformed and is the only pathway for the anticipated lower crustal flow from central Tibet (Royden et al., 1997; Clark & Royden, 2000). A large-scale intracrustal low velocity zone (ICLVZ) (Yao et al., 2010; Bao et al., 2015, Peng et al., 2017, 2019), high electrical conductivity (Bai et al., 2010) and high Poisson's ratio (Wen et al., 2019) support the existence of a lower crustal flow system. The Pis-phase polarity illustrates the presence of an extensive ICLVZ (Fig. 4). However, there is certain discrepancy regarding the position and seismic impedance of this ICLVZ due to the non-uniqueness of the data inversion scheme. Nonetheless, its position is not limited to two arc-shaped channels described in previous studies (Bai et al., 2010; Bao et al., 2015), but is more consistent with the spatial distribution of Poisson's ratio (Wen et al., 2019). Most of the big earthquakes (Ms > 7.0) in the Yunnan region since 500 AD to 2017, such as the 1833 Songming earthquake (Ms 8.0) on the Xiaojiang fault, are located in the transition zone between high- and low-speed anomalies, while most of the more moderate events (Ms ~ 6.0) are in zones of low-speed anomalies (Fig. 4). This feature agrees with a previous study based on Pn anisotropic tomography (Lei et al., 2014), supports the Pis-phase negative polarity (Fig. 4, stations in red) and is reliable evidence of the existence of a wide ICLVZ in the Yunnan region.

The average splitting time of 0.72 s for the lower crust in CYB is the largest among all the tectonic units (Table 2); combined with the aforementioned ICLVZ suggests the existence of a strong shear zone associated with the lower crustal flow. The Pn anisotropic tomography-based study performed by Lei et al. (2014) has revealed an approximate N-S trend of the fast Pn-wave velocity and large-scale low-speed anomalies below CYB, indicating a high temperature near the Moho. High-temperature at crustal depth suggests that the lattice preferred orientation (LPO) of amphibole is Type II or Type III (Ko & Jung, 2015; Kong et al., 2016), being the FPDs sub-parallel to the flow direction. Thus, the FPDs predominantly oriented NW-SE (Fig. 5b) and the ICLVZ in CYB provide additional evidence for the existence of a lower crustal flow channel. The predominant orientation NW-SE of the FPDs relative to the more or less thick upper crust of ~21 km (Fig. 4) is consistent with the lower crustal flow anticipated by Clark & Royden (2000) and Clark et al. (2005). This may be the result of resistance to the expansion of the flow to the southeast due to the tectonically stable South China block.

There are also other possible anisotropy-generating mechanisms, namely: fluid flow in the lower crust, vertical structures that cut internal shear zones, or vertically aligned rock volumes with alternating hydration levels, specifically alternating amphibolite and granulite rock masses (Zheng et al., 2018). Besides the aforementioned contributors, shear-related mineral lineation may be a possible contributor to the anisotropy observed in CYB due to the existence of great strike-slip faults.

To the north of EYB, previous studies (Wang et al., 2014) revealed that the south margin of the Sichuan basin experienced right-lateral shearing over a wide zone along the Huayinshan fault (F1 in Fig. 1). The shear velocity structure (Peng et al., 2017, 2019) and the results obtained in this study demonstrate that there is a small-scale ICLVZ and none earthquake with Ms > 6.0 (Fig. 4). The reason may be that the ICLVZ is too thin to accumulate enough seismic energy. We have 24 two-layer anisotropy measurements: the average splitting time of 0.70 s for the lower crust (Table 2) implies the existence of strong shearing, while the fault-parallel FPDs (Fig. 5b) indicate a tight relation between the observed anisotropy and the fractures in the shear zone. Thus, shearing in the fault zone may be the main source of anisotropy in the lower crust. Nonetheless, the dominant NW-SE orientation of FPDs in the upper crust could be attributed to the orthogonal compression stress induced by the southeastward extrusion from eastern Tibet.

4.5. Deformation of the lower crust on the west side of the Jinshajiang-Red River fault

The Indochina block began to extrude towards the southeast in the early stages of the continental collision between the Indian and Eurasian plates (Tapponnier et al., 1982, 2001), and during the Oligo-Miocene it moved southeastward at least 500 km along the Jinshajiang-Red River fault (Tapponnier et al., 1990). In the lower crust, a sharp contrast in FPDs is observed between LSB and TBB, with polarization directions oriented predominantly NW-SE (142º) in LSB and N-S (57º) in TBB (Figure 5b, Table 2). In LSB, the FPDs are inconsistent with the maximum horizontal compression stress, but are consistent with the strike of the faults, so the lower crust anisotropy may be the result of fractures in the faulting zone. Moreover, the FPDs oriented NW-SE in LSB (which were determined at 6 stations) seem to reflect the early extrusion of Tibet to the southeast, resulting in a lower crustal flow from central Yunnan toward the Indochina block, rotating clockwise around EHS, as anticipated by Bai et al. (2010) and Bao et al. (2015).

In TBB, other studies (Bao et al, 2015; Peng et al., 2017, 2019) and also this study reveal a wide ICLVZ in the Tengchong volcano area (Fig. 4), whose last eruption occurred in 1603 and gave rise to a high heat flow of 110 mW/m2 (Hu et al., 2000). A high value of Poisson's ratio is also observed (Hu et al., 2018; Wen et al., 2019). The combination of these features might involve partial melting of the crust. Nonetheless, recent studies reveal that the source of the Tengchong volcano comes from the mantle transition zone, about 100-200 km to the east (Zhang et al., 2017; Xu et al., 2018). The formation of the Tengchong volcano is not only related to the northeastward subduction of the Indian plate and the upwelling of partially melt mantle materials, but is also controlled by the rifting process due to the trench rollback of the Indian plate (Wang et al., 1998; Lei et al., 2009).

The comparatively small splitting times for the lower crust (0.43 s, Table 2) suggest the absence of shearing, and similar FPDs in the upper and lower crust (77º and 57º respectively, Table 2) indicate that both layers may be coupled to each other. Because the average FPD in this area (57º, Table 2) is roughly sub-parallel to the northeastward subduction of the Indian plate below Burma, we speculate that the principal cause of the observed anisotropy in the lower crust is the LPO of anisotropic minerals associated with the plastic flow induced by the trench rollback. Shear-related mineral lineation can also be a possible contributor to anisotropy due to the existence of major faults such as the Lancangjiang fault, the Jiali-Nujiang fault and the Sagaing fault.

5. Conclusions

P-to-S converted phases at the Moho and an intracrustal discontinuity are applied to study the structure and seismic anisotropy of the crust in the southeast margin of Tibet. Our results revealed the existence of a widespread of ICLVZ and two-layer crust structure in the study area. Furthermore, both the upper and lower crust are remarkably anisotropic, so that it may be inappropriate to simply attribute the anisotropy source causing the Pms splitting to the lower crust. In addition, the crustal anisotropy results show significant differences between the upper and lower crust, the FPDs in the upper crust are dominantly consistent with the regional compress fields, suggesting that the extensional fluid-saturated microcracks induced by the rigid extrusion from the central Tibet are mostly responsible for the observed upper crustal anisotropy. On the east side of the Jinshajiang-Red River fault, a widespread of ICLVZ and the FPDs oriented dominantly NW-SE in the lower crust beneath the CYB provide additional evidence for the existence of a lower crustal channel flow. On the west side of the Jinshajiang-Red River fault, a sharp contrast in the anisotropic parameters indicates that the lower crustal anisotropy in the LSB is mostly related to the NW-SE fractures in fault zone, while the LPO of anisotropic minerals associated with the plastic flow mostly contributor to the lower crustal anisotropy in the TBB.

The observed lower crustal anisotropy and widespread ICLVZ in the study area support the existence of the southeastward lower crustal flow, while this flow is not limited into two arcuate channels, furthermore, it did not penetrate the Jinshajiang-Red River fault from the CYB to the Indochina block. We conclude that the in-block rigid extrusion of the upper crust and the lower crustal flow may not be irreconcilable modes of crustal deformation. Nonetheless, it is difficult to accurately visualize the flow shape due to the small number of stations located in the Central Yunnan block and the available data collected in the course of one or two years.

Acknowledgements

The China Seismic Array Data Management Center, Institute of Geophysics, China Earthquake Administration (ChinArray DMC, doi:10.12001/ChinArray.Data, http://www.chinarraydmc.cn/), provided us the basic data used in this study, so we would like to thank Dr. Weilai Wang for his cooperation. We are also grateful to two anonymous reviewers for their helpful comments and constructive suggestions that made possible a better presentation of this paper. The National Natural Science Foundation of China provided financial support for this research work (grant 41774110).

References

Allen, C.R., Luo, Z.L., Qian, H., Wen, X.Z., Zhou, H.W., Huang, W.S., 1991. Field study of a highly active fault zone: the Xianshuihe fault of southwestern China. Geological Society of America Bulletin 103 (9), 1178-1199.

Ammon, C.J., 1991. The isolation of receiver effects from teleseismic P waveforms. Bulletin of the Seismological Society of America 81, 2504-2510.

Bai, D., Unsworth, M., Meju, M., Ma, X., Teng, J., Kong, X., Sun, Y., Sun, J., Wang, L., Jiang, C., Zhao, C., Xiao, P., Liu, M., 2010. Crustal deformation of the eastern Tibetan Plateau revealed by magnetotelluric imaging. Nature Geoscience 3, 358-362.

Bao, X., Sun, X., Xu, M., Eaton, D.W., Song, X., Wang, L., Ding, Z., Mi, N., Li, H., Yu, D., Huang, Z., Wang, P., 2015. Two crustal low-velocity channels beneath SE Tibet revealed by joint inversion of Rayleigh wave dispersion and receiver functions. Earth and Planetary Science Letters 415, 16-24.

Brocher, T.M., Christensen, N.I., 1990. Seismic anisotropy due to preferred mineral orientation observed in shallow crustal rocks in southern Alaska. Geology 18, 737-740.

Burlini, L., Fountain, D.M., 1993. Seismic anisotropy of metapelites from the Ivrea-Verbano zone and Serie dei Laghi (northern Italy). Physics of the Earth and Planetary Interior 78, 301-317.

Cai, Y., Wu, J., Fang, L., Wang, W., Yi, S., 2016. Crustal anisotropy and deformation of the southeast margin of the Tibetan Plateau revealed by Pms splitting. Journal of African Earth Sciences 121, 120-126.

Chang, L.J., Wang, C.Y., Ding, Z.F., You, H.C., Lou, H., Shao, C.R., 2015. Upper mantle anisotropy of the eastern Himalayan syntax and surrounding regions from shear wave splitting analysis. Science in China, Series D-Earth Sciences 58 (10), 1872-1882.

Chen, Y., Zhang, Z., Sun, C., Badal, J., 2013. Crustal anisotropy from Moho converted Ps wave splitting analysis and geodynamic implications beneath the eastern margin of Tibet and surrounding regions. Gondwana Research 24, 946-957.

Clark, M.K., Royden, L.H., 2000. Topographic ooze: Building the eastern margin of Tibet by lower crustal flow. Geology 28 (8), 703-706.

Clark, M.K., House, M.A., Royden, L.H., Whipple, K.X., Burchfiel, B.C., Zhang, X., Tang, W., 2005. Late Cenozoic uplift of southeast Tibet. Geology 33(6), 525-528.

Crampin, S., 1981. A review of wave motion in anisotropic and cracked elastic-media. Wave Motion 3, 343-391.

Crampin, S., 1994. The fracture criticality of crustal rocks. Geophysical Journal International 118, 428-438.

Dueker, K.G., Sheehan, A.F., 1997. Mantle discontinuity structure form midpoint stacks of converted P to S waves across the Yellowstone hotspot tract. Journal of Geophysical Research 102, 8313-8327.

Dueker, K.G., Sheehan, A.F., 1998. Mantle discontinuity structure beneath the Colorado Rocky Mountains and High Plains. Journal of Geophysical Research 103, 7153-7169.

England, P.C., Houseman, G.A., 1988. The mechanics of the Tibetan Plateau. Royal Society of London Philosophical Transactions, ser. A 326, 301-320.

England, P., Molnar, P., 1997. Active deformation of Asia: from kinematics to dynamics. Science 278, 647-650.

Flesch, L.M., Holt, W.E., Silver, P.G., Stephenson, M., Wang, C.Y., Chan, W.W., 2005. Constraining the extent of curst–mantle coupling in central Asia using GPS, geologic, and shear wave splitting data. Earth and Planetary Science Letters 238, 248-268.

Gan, W., Zhang, P., Shen, Z.K., Niu, Z., Wang, M., Wan, Y., Zhou, D., Cheng, J., 2007. Present-day crustal motion within the Tibetan Plateau inferred from GPS measurements. Journal of Geophysical Research Solid Earth 112, B08416.

Hu, J., Badal, J., Yang, H., Li, G., Peng, H., 2018. Comprehensive crustal structure and seismological evidence for lower crustal flow in the southeast margin of Tibet revealed by receiver functions. Gondwana Research 55, 42-59.

Hu, S.B., He, L.J., Wang, J.Y., 2000. Heat flow in the continental area of China: a new data set. Earth and Planetary Science Letters 179(2), 407-419.

Ji, J.Q., Zhong, D.L., Sang, H.Q. Zhang, L.S., 2000. The western boundary of extrusion blocks in the southeastern Tibetan Plateau. China Science Bulletin 45, 876-881.

Ji, S., Shao, T., Michibayashi, K., Oya, S., Satsukawa, T., Wang, Q., Zhao, W., Salisbury, M.H., 2015. Magnitude and symmetry of seismic anisotropy in mica- and amphibole-bearing metamorphic rocks and implications for tectonic interpretation of seismic data from the southeast Tibetan Plateau. Journal of Geophysical Research Solid Earth 120, 6404-6430.

Kennett, B., Engdahl, E.R., 1991. Travel times for global earthquake location and phase identification. Geophysical Journal International 105(2), 429-465.

King, R.W., Shen, F., Burchfiel, B.C., Royden, L.H., Wang, E., Chen, Z.L., Li, Y.P., Zhang, X.Y., Zhao, J.X., Li, Y.L., 1997. Geodetic measurement of crustal motion in southwest China. Geology 25 (2), 179-182.

Ko, B., Jung, H., 2015. Crystal preferred orientation of an amphibole experimentally deformed by simple shear. Nature Communications 6, 6586.

Kong, F., Wu, J., Liu, K. H., Gao, S., 2016. Crustal anisotropy and ductile flow beneath the eastern Tibetan Plateau and adjacent areas. Earth and Planetary Science Letters 442, 72–79.

Langston, C.A., 1977. Corvallis, Oregon, crustal and upper mantle structure from teleseismic P and S waves. Bulletin of the Seismological Society of America 67(3), 713-724.

Langston, C.A., 1979. Structure under Mount Rainer, Washington, inferred from teleseismic body waves. Journal of Geophysical Research 84(B9), 4749-4762.

Lei, J., Zhao, D., Su, Y., 2009. Insight into the origin of the Tengchong intraplate volcano and seismotectonics in southwest China from local and teleseismic data. Journal of Geophysical Research 114, B05302.

Lei, J., Li, Y., Xie, F., Teng, J., Zhang, G., Sun, C., Zha, X., 2014. Pn anisotropic tomography and dynamics under eastern Tibetan Plateau. J. Geophys. Res. Solid Earth 119(3), 2174-2198.

Leloup, P.H., Lacassin, R., Tapponnier, P., Scharer, U., Zhong, D.L., Liu, X.H., Zhang, L. S., Ji, S., Trinh, P.T., 1995. The Ailao Shan-Red River shear zone (Yunnan, China), Tertiary transform boundary of Indochina. Tectonophysics 251, 3-84.

Lev, E., Long, D.M., van der Hilst, R.D., 2006. Seismic anisotropy in Eastern Tibet from shear wave splitting reveals changes in lithospheric deformation. Earth and Planetary Science Letters 251, 293-304.

Levin, V., Roecker, S., Graham, P., Hosseini, A., 2008. Seismic anisotropy indicators in Western Tibet: shear wave splitting and receiver function analysis. Tectonophysics 462, 99-108.

Ligorria, J. P., Ammon, C.J., 1999. Iterative deconvolution and receiver-function estimation. Bulletin of the Seismological Society of America 89, 1395-1400.

Mainprice, D., Nicolas, A., 1989. Development of shape and lattice preferred orientations: application to the seismic anisotropy of the lower crust. Journal of Structural Geology 11(1), 175-189.

Molnar, P., Tapponnier, P., 1975. Cenozoic tectonics of Asia: effects of a continental collision. Science 189, 419-426.

Okaya, D., Christensen, N., Stanley, D., Stern, T., 1995. Crustal anisotropy in the vicinity of the Alpine Fault Zone. New Zealand Journal of Geology and Geophysics 38, 579-583.

Peng, H., Yang, H., Hu, J., Badal, J., 2017. Three-dimensional S-velocity structure of the crust in the southeast margin of the Tibetan plateau and geodynamic implications. Journal of Asian Earth Sciences 148, 210-222.

Peng, H., Hu, J., Badal, J., Yang, H., 2019. S-wave velocity images of the crust in the southeast margin of Tibet revealed by receiver functions. Pure and Applied Geophysics https://doi.org/10.1007/s00024-019-02178-4.

Royden, L.H., Burchfiel, B.C., King, R.W., Wang, E.C., Chen, Z.L., Shen, F., Liu, Y.P., 1997. Surface deformation and lower crustal flow in Eastern Tibet. Science 276 (2), 788-790.

Royden, L.H., Burchfiel, B.C., van der Hilst, R.D., 2008. The geological evolution of the Tibetan Plateau. Science 321, 1054-1058.

Rümpker, G., Kaviani, A., Latifi, K., 2014. Ps-splitting analysis for multilayered anisotropic media by azimuthal stacking and layer stripping. Geophysical Journal International 199, 146-163.

Savage, M.K., 1999. Seismic anisotropy and mantle deformation: what have we learned from shear wave splitting? Reviews of Geophysics 37, 65-106.

Savage, M.K. Peppin, W.A., Vetter, U.R., 1990. Shear wave anisotropy and stress direction in and nar Long Valley Caldera, California, 1979-1988. Journal of Geophysical Research 95, 11165-11177.

Shi, Y., Gao, Y., Su, Y., Wang, Q., 2012. Shear-wave splitting beneath Yunnan area of Southwest China. Earthquake Science 25 (1), 25-34.

Sol, S., Meltzer, A.S., Bürgmann, R., van der Hilst, R.D., King, R., Chen, Z., Koons, P.O., 2007. Geodynamics of the southeast Tibetan Plateau from seismic anisotropy and geodesy. Geology 35 (6), 563-566.

Sun,Y., Niu, F., Liu, H., Chen, Y., Liu, J., 2012. Crustal structure and deformation of the SE Tibetan plateau revealed by receiver function data. Earth and Planetary Science Letters 349-350, 186-197.

Sun, Y., Liu, J., Zhou, K., Chen, B., Gao, R., 2015. Crustal structure and deformation under the Longmenshan and its surroundings revealed by receiver function data. Physics of the Earth and Planetary Interiors 244, 11-22.

Tapponnier, P., Peltzer, G., Le Dain, A.Y., Armijo, R., Cobbold, P., 1982. Propagating extrusion tectonics in Asia: New insights from simple experiments with plasticine. Geology 10, 611-616.

Tapponnier, P., Lacassin,R., Leloup, P.H., Scharer, U., Zhong, D., Wu, H., Liu, X., Ji, S., Zhang, L., Zhong, J., 1990. The Ailao Shan/Red River metamorphic belt: tertiary left-lateral shear between Indochina and South China. Nature 343, 431-437.

Tapponnier, P., Zhiqin, X., Roger, F., Meyer, B., Arnaud, N., Wittlinger, G., Jingsui, Y., 2001. Oblique stepwise rise and growth of the Tibet Plateau. Science 294, 1671-1677.

Tatham, D. J., Lloyd, G. E., Butler, R., Casey, M., 2008. Amphibole and lower crustal seismic properties. Earth and Planetary Science Letters 267, 118-128.

Vera, S.P., Mahan, K.H., 2014. A method for mapping crustal deformation and anisotropy with receiver functions and first results from USArray. Earth and Planetary Science Letters 402, 221-233.

Vinnik, L.P., 1977. Detection of waves converted from P to SV in the mantle. Physics of the Earth and Planetary Interiors 15, 39-45.

Wang, E., Burchfiel, B.C., Royden, L.H., Chen, L., Chen, J., Li, W., Chen, Z., 1998. Late Cenozoic Xianshuihe-Xiaojiang, Red River, and Dali Fault Systems of Southwestern Sichuan and Central Yunnan, China. Geological Society of America special paper, 327.

Wang, C.Y., Flesch, L.M., Silver, P.G., Chang, L.J., Chan, W., 2008. Evidence for mechanically coupled lithosphere in central Asia and resulting implications. Geology 36 (5), 363-366.

Wang, E., Meng, K., Su, Z., Meng, Q., Chu, J.J., Chen, Z., Wang, G., Shi, X., Liang, X., 2014. Block rotation: Tectonic response of the Sichuan basin to the southeastward growth of the Tibetan Plateau along the Xianshuihe-Xiaojiang fault. Tectonics 33, 686-717.

Wang, Q. Niu, F., Gao, Y., Chen, Y., 2016. Crustal structure and deformation beneath the NE margin of the Tibetan plateau constrained by teleseismic receiver function data. Geophysical Journal International 204, 167-179.

Wen, L., Badal, J., Hu, J., 2019. Anisotropic *H-k* stacking and (revisited) crustal structure in the southeastern margin of Tibet. Journal of Asian Earth Sciences 169, 93-104.

Wessel, P., Smith, W., 1998. New, improved version of generic mapping tools released. Eos Transactions 79, 579-579.

Wu, J., Zhang, Z., Kong, F., Yang, B.B., Yu, Y., Liu, K.H., Gao, S.S., 2015. Complex seismic anisotropy beneath western Tibet and its geodynamic implications. Earth and Planetary Science Letters 413, 167–175.

Xu, M., Huang, H., Huang, Z., Wang, P., Wang, L., Xu, M., Mi, N., Li, H., Yu, D., Yuan, X., 2018. Insight into the subducted Indian slab and origin of the Tengchong volcano in SE Tibet from receiver function analysis. Earth and Planetary Science Letters 482, 567-579

Yang, Y., Zhu, L., Su, Y., Chen, H., Wang, Q., Zhang, P., 2015. Crustal anisotropy estimated by splitting of Ps-converted waves on seismogram and an application to SE Tibetan Plateau. Journal of Asian Earth Sciences 106, 216–228.

Yao, H., van der Hilst, R.D., Montagner, J.P., 2010. Heterogeneity and anisotropy of the lithosphere of SE Tibet from surface wave array tomography. Journal of Geophysical Research 115, B12307.

Yin, A., 2000. Mode of Cenozoic east-west extension in Tibet suggesting a common origin of rifts in Asia during the Indo-Asian collision. Journal of Geophysical Research 105, 21745-21759.

Yin, A., Harrison, T.M., 2000. Geologic evolution of the Himalayan-Tibetan orogen. Annual Review of Earth and Planetary Sciences 28, 211-280.

Zhang, P.Z., Shen, Z., Wang, M., Gan, W., 2004. Continuous deformation of the Tibetan Plateau from Global Positioning System data. Geology 32, 809- 812.

Zhang, R., Wu, Y., Gao, Z., Fu, Y. V., Sun, L., Wu, Q., Ding, Z., 2017. Upper mantle discontinuity structure beneath eastern and southeastern Tibet: New constraints on the Tengchong intraplate volcano and signatures of detached lithosphere under the western Yangtze Craton. Journal of Geophysical Research Solid Earth 122, 1367–1380.

Zhang, X. and Wang, Y., 2009. Crustal and upper mantle velocity structure in Yunnan, Southwest China. Tectonophysics 471, 171-185.

Zheng, D. C., Saygin, E., Cummins, P., Ge, Z., Min, Z., Cipta, A.,Yang, R., 2017. Transdimensional Bayesian seismic ambient noise tomography across SE Tibet. Journal of Asian Earth Sciences 134, 86–93.

Zheng, T., Ding, Z., Ning, J., Chang, L., Wang, X., Kong, F., 2018. Crustal azimuthal anisotropy beneath the southeast Tibetan Plateau and its geodynamic implications. J. Geophys. Res. Solid Earth 123, https://doi.org/10.1029/2018JB015995.

Zhu, L., Kanamori, H., 2000. Moho depth variations in southern California from teleseismic receiver functions. Journal of Geophysical Research 105(B2), 2969-2980.

Table 1. Disaggregated anisotropy parameters estimated by Pis and Pms splitting for the upper and lower crust.

Station code	δt_1	Uncertainty in δt_1	ϕ_1	Uncertainty in ϕ_1	δt_2	Uncertainty in δt_2	ϕ_2	Uncertainty in ϕ_2
HLT	0.71	0.08	20	3	1.13	0.09	-86	3
YIM	0.38	0.05	90	2	0.79	0.08	-17	3
TOH	0.41	0.07	-82	5	0.42	0.07	-2	5
53057	1.34	0.1	-11	2	1.09	0.1	73	2
53224	1.25	0.1	-22	2	0.65	0.08	51	3
53028	1.15	0.1	74	2	0.87	0.09	-16	2
52032	1.1	0.09	-46	3	1.2	0.1	48	2
53173	1.09	0.1	9	2	0.76	0.08	-79	3
53230	1	0.1	-54	0	0.5	0.1	39	3
51051	0.97	0.09	-63	3	0.06	0.09	-9	3
53216	0.97	0.09	-34	2	1.27	0.1	55	2
53236	0.97	0.09	-34	2	1.27	0.1	55	2
53105	0.87	0.09	60	3	1.06	0.09	-39	3
53164	0.82	0.09	-46	3	0.71	0.08	42	4
53160	0.81	0.09	-25	3	0.59	0.08	59	4
53227	0.78	0.09	41	3	0.89	0.09	-56	3
51030	0.76	0.08	-34	3	1.13	0.1	39	3
53231	0.74	0.08	-8	3	1.26	0.1	59	2
53042	0.72	0.08	65	3	0.86	0.09	-14	3
53090	0.72	0.08	58	3	0.86	0.12	23	2
53223	0.71	0.08	-84	3	1.39	0.11	0	2
51019	0.7	0.08	4	3	0.95	0.09	76	3
52026	0.65	0.07	-54	4	0.88	0.08	1	2
51055	0.63	0.1	-68	2	1.1	0.11	24	2
51020	0.61	0.08	-74	4	1.14	0.1	28	2
53213	0.6	0.08	23	4	0.86	0.09	-66	3
51058	0.59	0.08	-22	4	0.75	0.08	81	4
53081	0.58	0.09	78	3	0.53	0.08	14	4
51014	0.57	0.08	85	4	0.66	0.08	-6	3
53228	0.56	0.08	-92	4	0.5	0.07	1	4
53083	0.55	0.07	40	5	0.49	0.07	49	4
51035	0.55	0.08	-60	4	0.45	0.07	57	5
51048	0.53	0.07	-74	4	0.54	0.08	-13	4
51057	0.53	0.08	-80	4	1.19	0.1	12	2
53063	0.52	0.07	56	4	0.28	0.07	-45	7
51034	0.51	0.08	-8	4	0.99	0.09	85	2
53235	0.51	0.07	55	4	0.95	0.09	9	3
51011	0.5	0.08	-31	4	0.96	0.09	63	3
53058	0.49	0.1	89	0	0.33	0.07	-29	6

53172	0.48	0.07	61	4	0.21	0.07	-25	9
53005	0.47	0.07	-62	4	0.48	0.08	-38	3
53065	0.47	0.07	-55	5	0.74	0.08	53	3
53099	0.47	0.07	-69	5	0.54	0.07	41	5
53107	0.47	0.07	22	5	0.44	0.07	-52	5
51010	0.47	0.07	48	4	0.21	0.06	44	7
53222	0.46	0.07	62	5	0.29	0.07	-69	7
53097	0.45	0.07	-63	5	0.35	0.07	36	6
53061	0.43	0.07	33	5	0.17	0.07	2	10
53002	0.4	0.07	-30	3	0.55	0.08	-55	2
53046	0.39	0.07	36	5	0.67	0.08	-53	4
53233	0.39	0.07	-12	5	0.38	0.07	72	5
53034	0.37	0.07	-75	5	0.95	0.09	-73	3
53015	0.36	0.06	-15	5	0.07	0.06	28	21
51026	0.35	0.07	-63	6	0.23	0.06	46	9
53159	0.34	0.07	55	6	0.23	0.07	57	8
53084	0.33	0.08	75	5	0.48	0.07	14	5
53121	0.33	0.07	27	6	0.13	0.06	-56	14
53098	0.32	0.07	-71	7	0.24	0.07	61	8
53011	0.32	0.06	-88	6	0.82	0.08	-22	3
53232	0.32	0.07	-73	6	0.68	0.08	8	3
51006	0.31	0.07	-81	7	0.3	0.07	-21	6
53237	0.3	0.07	10	7	0.57	0.08	69	4
53049	0.29	0.06	-42	8	0.64	0.09	81	3
51007	0.25	0.07	81	8	0.3	0.07	11	7
53120	0.24	0.06	-67	8	0.37	0.07	-67	8
51004	0.2	0.07	-30	9	0.44	0.07	-65	5
51009	0.18	0.07	-86	10	0.48	0.08	9	4
51012	0.18	0.06	-61	10	0.67	0.08	55	3
52037	0.18	0.05	63	10	0.71	0.07	-25	3
51003	0.15	0.06	11	13	0.29	0.07	87	7
53100	0.12	0.07	61	15	0.42	0.08	76	4
53221	0.11	0.06	-74	18	0.56	0.08	-38	4
51054	0.08	0.07	79	22	0.34	0.07	-45	6
51008	0.07	0.07	80	26	0.55	0.08	33	4
51050	0.05	0.07	-50	36	1.14	0.1	64	2

δt is delay time in seconds; φ is fast wave polarization direction. The subscripts 1 and 2 refer to the upper crust and the lower crust, respectively.

Table 2. Averaged shear wave splitting parameters (fast polarization direction and delay time) that characterize the disaggregated anisotropy of the upper and lower crust in different tectonic blocks.

Tectonic block	Anisotropy of the upper crust		Anisotropy of the lower crust	
	FPD (°)	Splitting time (s)	FPD (°)	Splitting time (s)
EYB	98±48	0.55±0.29	70±50	0.70±0.33
CYB	103±40	0.51±0.31	102±50	0.72±0.34
LSB	83±48	0.63±0.27	142±16	0.63±0.31
TBB	77±33	0.43±0.15	57±42	0.43±0.20

EYB, Eastern Yunnan block; CYB, Central Yunnan block; LSB, Lanping-Simao block; TBB, Tengchong-Baoshan block.

Figures and legends

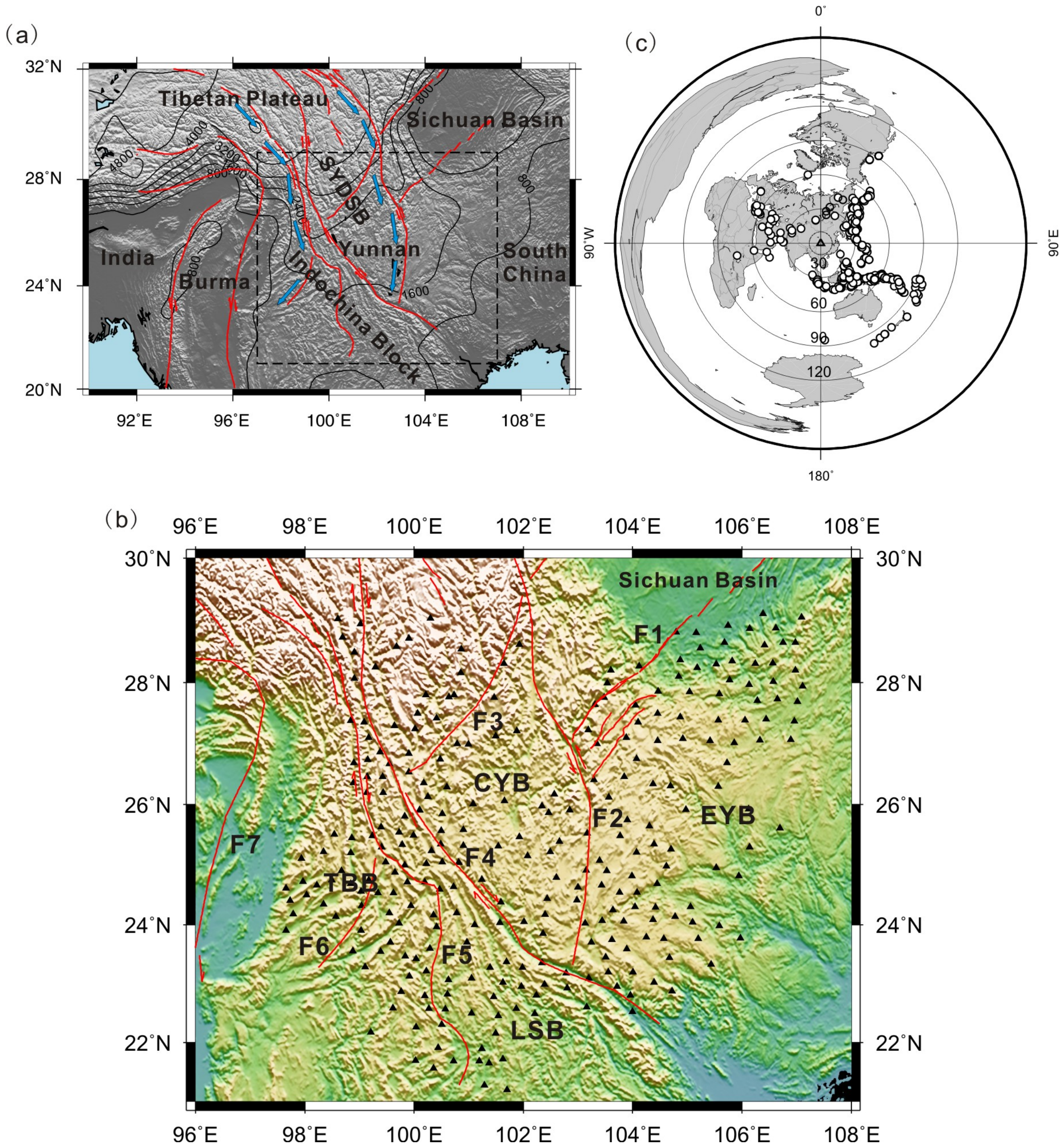

Figure 1. (a) Geographic map of South Asia where the study region is contoured by a rectangle and the terrain elevation is indicated by isolines drawn at intervals of 800 m. The acronym SYDSB denotes the Sichuan-Yunnan diamond-shaped block. Blue arrows indicate possible crustal flow channels (Bai et al., 2010). (b) Major active faults (red lines) and broadband stations (triangles) deployed in southeast Tibet and nearby areas. Key to symbols: F1, Huayinshan fault; F2, Xianshuihe-Xiaojiang fault; F3, Lijiang-Jinhe fault; F4, Jinshajiang-Red River fault; F5, Lancangjiang fault; F6, Jiali-Nujiang fault; F7, Sagaing fault; TBB, Tengchong-Baoshan block; CYB, Central Yunnan block; EYB, Eastern Yunnan block; LSB, Lanping-Simao block. (c) Locations of the earthquakes used in this study on a worldwide map. The small triangle in the center of the figure marks the location of the study region.

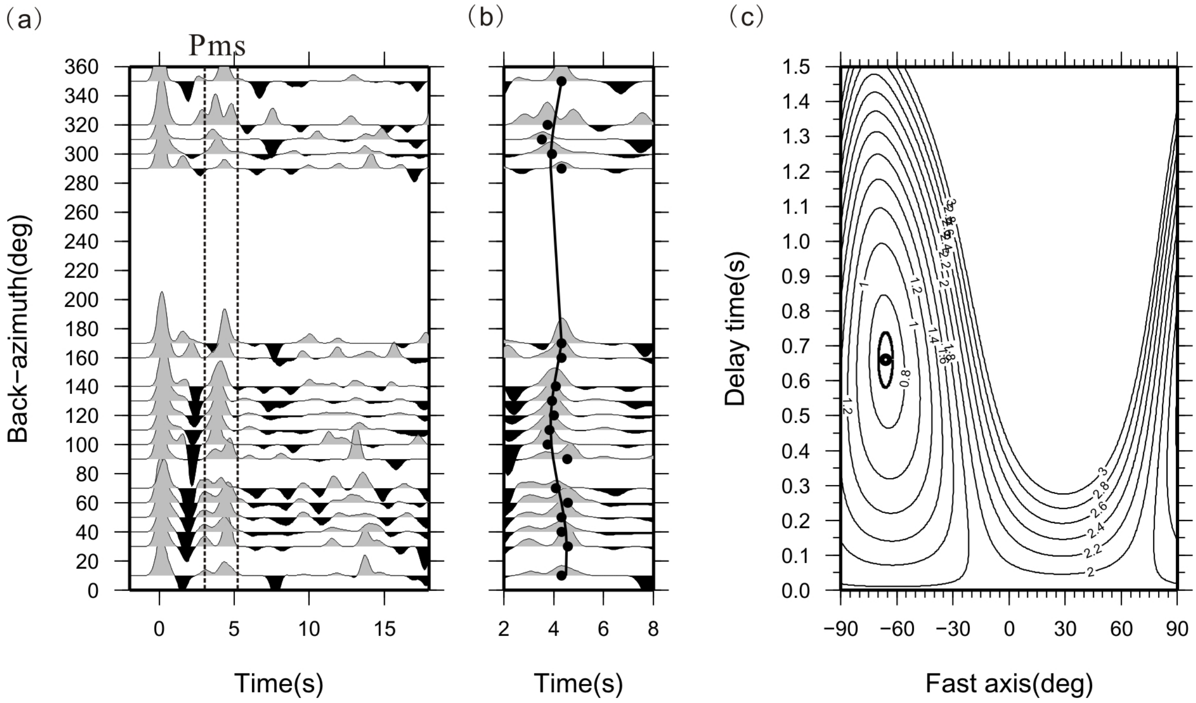

Figure 2. Receiver functions at station 53133 and fit of the Pms-wave splitting parameters. (a) Azimuthal gather of receiver functions; two vertical dotted lines mark Pms-wave arrivals. (b) Enlarged view of the arrival times of the Pms peaks (black dots); the thick line marks the theoretical arrival times calculated from the splitting parameters. (c) Traveltime variance diagram on the solution surface of splitting parameters; the black dot marks the solution for the splitting parameters given by the minimum variance of traveltime, while the small ellipse provides an estimation of the uncertainty in the splitting parameters.

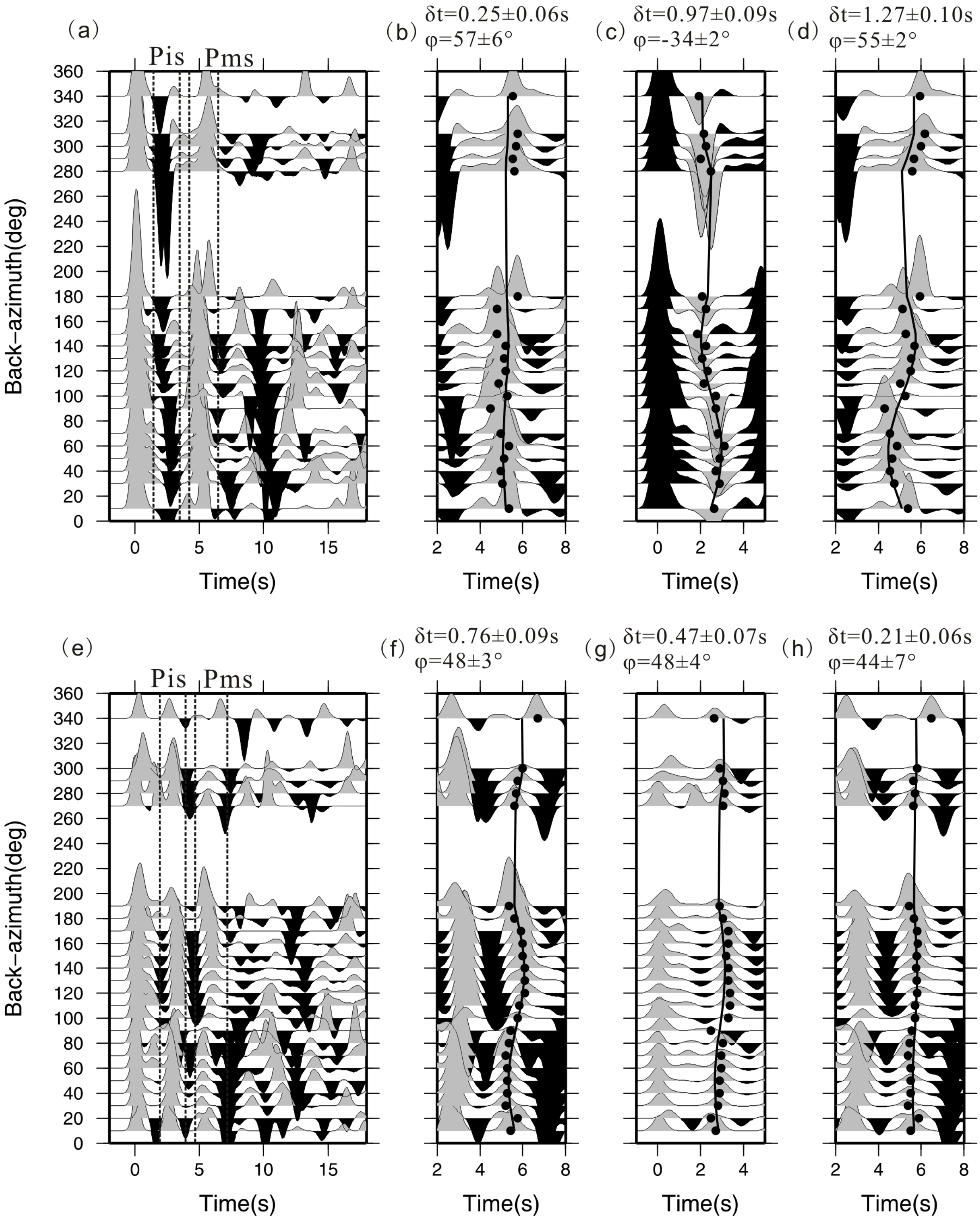

Figure 3. Double-layer crustal anisotropy measured at stations 53216 (a – d) and 51010 (e – h). (a and e) Plots showing respectively the 10º bin-averaged receiver functions versus the backazimuth, and the Pis and Pms arrivals (delimited by vertical dotted lines). (b and f) Enlarged views of the arrival times of the Pms peaks (black dots); the thick lines mark the theoretical arrival times calculated using the optimal anisotropy parameters obtained from the Pms phase. (c and g) Enlarged views of the arrival times of the Pis peaks (black dots);

now the thick lines mark the theoretical arrival times calculated using the optimal anisotropy parameters obtained from the Pis phase. (d and h) Pms arrival times (black dots); now the wavy lines mark the theoretical arrival times computed using the optimal anisotropy parameters obtained from the Pms phase after correcting for the upper crust anisotropy. Splitting delay times (δt) and polarization directions (φ) with 1σ-deviations are given on top of the corresponding plots.

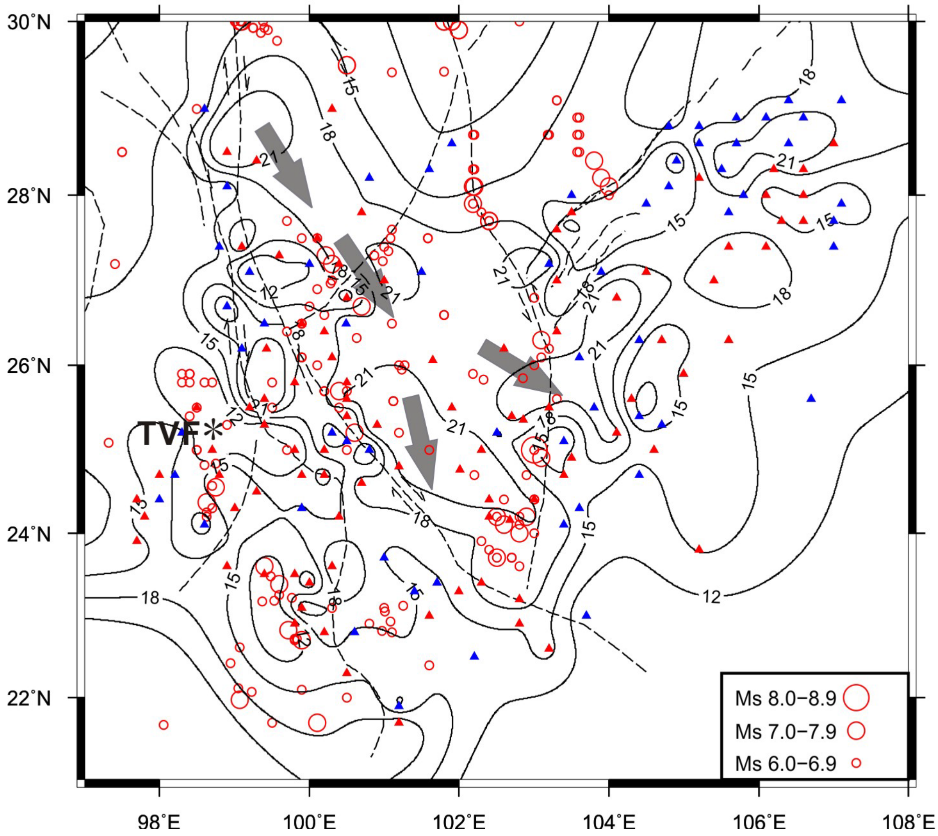

Figure 4. Upper crust thickness mapped by spline interpolation using the GMT software (Wessel & Smith, 1998); the contour lines are drawn at 3 km intervals. The small triangles indicate the locations of the broadband stations used in this study: red triangles mean that there is an interface with negative seismic velocity contrast below the corresponding station, while blue triangles mean a positive velocity contrast. The red circles represent earthquakes with Ms ≥ 6.0 (bottom right corner) that have occurred in the southeast of Tibet since 500 AD to 2017. The gray arrows denote the lower crustal flow. TVF is the acronym for Tengchong volcano field.

(a)

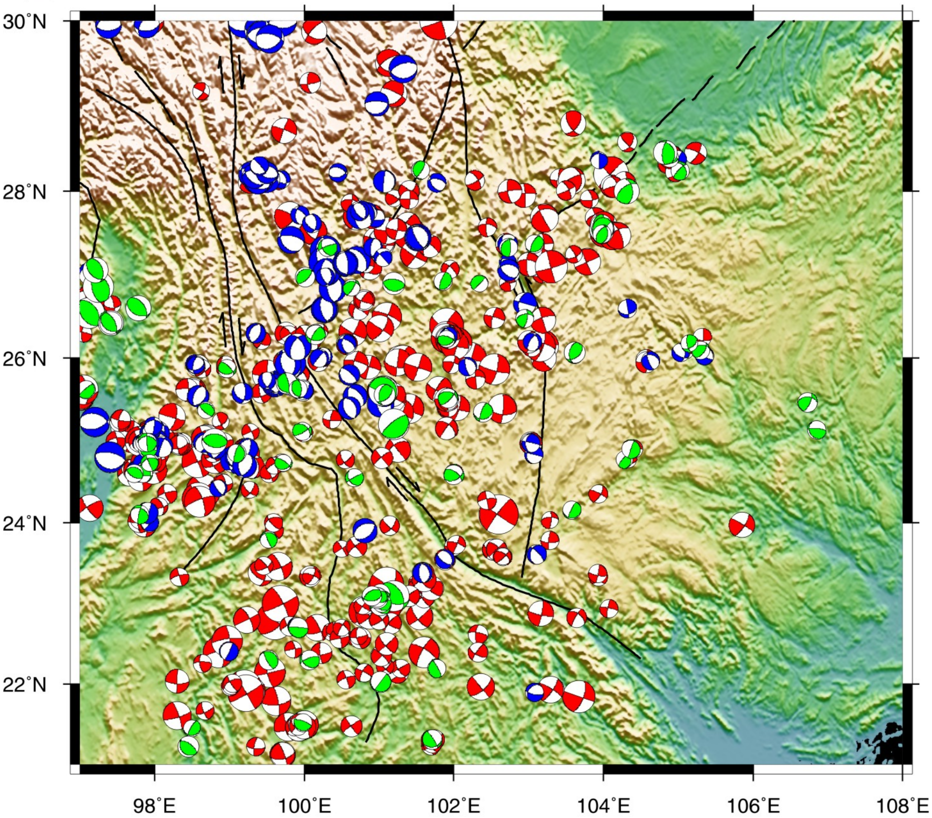
30°N
28°N
26°N
24°N
22°N
98°E
100°E
102°E
104°E
106°E
108°E

(b)

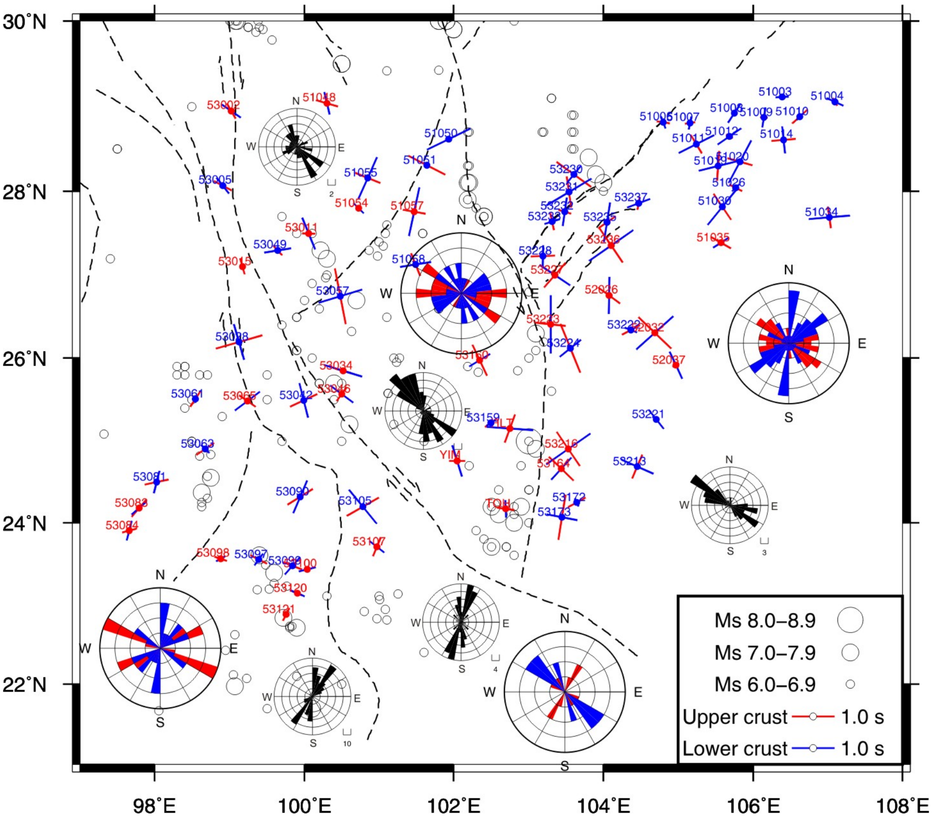
30°N
28°N
26°N
24°N
22°N
98°E
100°E
102°E
104°E
106°E
108°E
Ms 8.0–8.9
Ms 7.0–7.9
Ms 6.0–6.9
Upper crust 1.0 s
Lower crust 1.0 s

Figure 5. (a) Focal mechanism solutions calculated for earthquakes with Ms ≥ 4.0 that have occurred in the southeast of Tibet since 1965 AD to 2017. (b) Comparison between upper crust anisotropy estimated by Pis splitting (red bars) and lower crust anisotropy measured from Pms splitting after correcting for the upper crust anisotropy (blue bars). The scale for splitting times is the same in both cases (bottom right corner). The dots show the locations of the seismic stations and the numbers are their respective station codes; blue or red colors indicate positive or negative polarity of the Pis phase, respectively. The circles represent earthquakes with Ms ≥ 6.0 (bottom right corner) since 500 AD to 2017. The black rose diagrams show the maximum horizontal compression stress for different tectonic blocks, while the red and blue rose diagrams show the fast wave polarization directions in the upper and lower crust, respectively. The dashed lines represent major faults.